HHS Public Access

Author manuscript

J Magn Reson Imaging. Author manuscript; available in PMC 2022 March 01.

Published in final edited form as:

J Magn Reson Imaging. 2021 March ; 53(3): 686–702. doi:10.1002/jmri.27070.

Fast Imaging for Hyperpolarized MR Metabolic Imaging

Jeremy W. Gordon, PhD[1], **Hsin-Yu Chen, PhD**[1], **Nicholas Dwork, PhD**[1], **Shuyu Tang, PhD**[1,2], **Peder E. Z. Larson**[1,2]

[1]Department of Radiology and Biomedical Imaging, University of California - San Francisco, San Francisco, CA, USA

[2]UC Berkeley/UCSF Graduate Program in Bioengineering

Abstract

MRI with hyperpolarized carbon-13 agents has created a new type of non-invasive, in vivo metabolic imaging that can be applied in cell, animal, and human studies. The use of ^{13}C labeled agents, primarily [1-^{13}C]pyruvate, enables monitoring of key metabolic pathways with the ability to image substrate and products based on their chemical shift. Over 10 sites worldwide are now performing human studies with this new approach for studies of cancer, heart disease, liver disease and kidney disease. Hyperpolarized metabolic imaging studies must be performed within several minutes following creation of the hyperpolarized agent due to irreversible decay of the net magnetization back to equilibrium, so fast imaging methods are critical. The imaging methods must also include multiple metabolites, separated based on their chemical shift, which are also undergoing rapid metabolic conversion (via label exchange), further exacerbating the challenges of fast imaging.

This review describes the state-of-the-art in fast imaging methods for hyperpolarized metabolic imaging. This includes the approach and tradeoffs between three major categories of fast imaging methods – fast spectroscopic imaging, model-based strategies, and metabolite specific imaging – as well additional options of parallel imaging, compressed sensing, tailored RF flip angles, refocused imaging methods, and real-time calibrations that can improve the scan coverage, speed, SNR, resolution, and/or robustness of these studies. To date, these approaches have produced extremely promising initial human imaging results. Improvements to fast hyperpolarized metabolic imaging methods will provide better coverage, SNR, resolution, and reproducibility for future human imaging studies.

Keywords

metabolic imaging; hyperpolarized carbon-13; spectroscopic imaging; chemical shift encoding; metabolite-specific imaging; real-time calibration

Corresponding Author: Peder Larson, PhD, 1700 4th St, Byers Hall Room 102C, San Francisco, CA 94143, Tel: 415-514-4876, peder.larson@ucsf.edu.

Introduction

MRI with hyperpolarized carbon-13 agents has created a new type of non-invasive, in vivo metabolic imaging that can be applied in cell, animal, and human studies (1). The use of ^{13}C labeled agents, primarily [1-^{13}C]pyruvate, enables monitoring of key metabolic pathways with the ability to image substrate and products based on their chemical shift. [1-^{13}C]pyruvate has been especially successful because its properties are well suited for hyperpolarized imaging studies (e.g. long T_1, high concentration preparations) and because of pyruvate's critical position in glycolysis, where it can either be used in TCA cycle metabolism or converted to lactate (Fig. 1). The conversion of pyruvate to lactate is preferentially upregulated in many types of cancers in a process referred to as the "Warburg effect", while normal differentiated cells prefer to use pyruvate in the TCA cycle (2). In the heart, the relative conversion of pyruvate going into the TCA cycle versus conversion to lactate is reflective of substrate selection between fatty acid and carbohydrate metabolism that is altered in many heart diseases. Altered pyruvate metabolism has also been studied pre-clinically in the context of traumatic brain injury (3,4), multiple sclerosis (5), liver disease (6), and diabetes (7), to name a few. Many other ^{13}C-labeled agents have been successfully developed in animal studies, including ^{13}C-urea as a measure of perfusion (8,9), ^{13}C-fumarate as a measure of necrosis (10), ^{13}C-alpha ketoglutarate as a measure of IDH status (11), ^{13}C-bicarbonate as a measure of extracellular pH (12), ^{13}C-butyrate as a measure of fatty acid metabolism (13), ^{13}C-dehydroascorbate as a measure of redox potential (14), and many more (15).

Human hyperpolarized (HP) ^{13}C MRI studies have used dissolution dynamic nuclear polarization (DNP) to create a solution with up to 100,000-fold increase in polarization compared to thermal equilibrium at room temperature and clinical MRI field strengths (16). In dissolution DNP, the ^{13}C-labeled substrate is mixed with an electron paramagnetic agent (EPA) and placed at low temperature (~1 K) and at high magnetic field (typically ≥5 T). Under these conditions, the free electron in the EPA is nearly 100% polarized, and microwave irradiation around the electron spin resonance frequency is applied to transfer this polarization to the ^{13}C nuclear spins to create a hyperpolarized state. After approximately 1–2 hours of microwave irradiation, the frozen mixture is rapidly dissolved with super-heated water and neutralized to physiologic pH, creating an agent suitable for injection. However, the hyperpolarized state is transient and relaxes to thermal Boltzmann equilibrium with time constant T_1 (e.g. for [1-^{13}C]pyruvate $T_1 \approx 50$ s in solution, $T_1 \approx 30$ s in vivo). This T_1 decay, as well as the rapid metabolic conversion (via ^{13}C label exchange), necessitates fast imaging techniques that can capture rapidly evolving signals within 1–2 minutes following injection.

This review will discuss the current state-of-the-art in fast imaging techniques for HP ^{13}C MR metabolic imaging. While dissolution DNP has been the primary polarization mechanism for human applications, the imaging strategies discussed here are equally amenable to hyperpolarization via other processes, such as PHIP or SABRE (17,18). These techniques can generally be grouped into three categories: (1) spectroscopic imaging; (2) model-based approaches; and (3) metabolite-specific imaging. The imaging speed typically increases from spectroscopic to metabolic-specific imaging, but with increasing constraints,

and are summarized in Fig. 2 and Table 1. The review will also cover several sequence options that can be combined with these imaging techniques, including parallel imaging and compressed sensing acceleration, tailored flip angles, spin refocusing methods, and real-time calibrations (summarized in Table 2.).

Fast Spectroscopic Imaging

Magnetic resonance spectroscopic imaging (MRSI) can provide spatial and spectral encoding to localize and resolve HP ^{13}C-labeled metabolites. MRSI techniques have the advantage that they provide a continuous spectrum which can be analyzed to extract expected as well as unexpected resonances, making this approach very robust and the go-to method for exploratory HP studies. The most straightforward method is phase-encoded CSI, which offers a large spectral bandwidth and high spectral resolution. However, the main challenge in performing hyperpolarized MRSI is imaging speed, and CSI is quite slow because it is a pure phase-encoded sequence. For example, CSI requires $N_x \times N_y$ RF excitations for a single slice, where $N_x \times N_y$ is the number of voxels in the 2D spatial array. Even a coarse 8 × 8 matrix requires 64 RF excitations, resulting in a long acquisition time (5+ seconds) for a single slice. It is most well-suited for pre-clinical studies with small FOVs (19,20) or for substrates with complicated spectra, such as [2-^{13}C]pyruvate (21), as its poor temporal resolution can hamper measurements of metabolic conversion and precludes volumetric coverage.

Rapid spectroscopic imaging techniques employing switched time-dependent or echo-planar type gradients applied during acquisition can greatly reduce the scan time for HP experiments compared to phase-encoded CSI. Joint spectral and spatial encoding is accomplished by traversing k-space at multiple TEs, shifted in time by ΔTE (Fig. 3). By acquiring the same k-space point (k_x, k_y) at multiple TEs, a Fourier transform along the echo dimension produces a spectrum at each k-space point, reducing the scan time by the number of acquired points in the frequency encoded dimension. The spectral and spatial encoding for rapid MRSI techniques with switched gradients can be achieved with arbitrary *k*-space trajectories, including echo-planar spectroscopic imaging (EPSI) (22), spiral (23), radial (24), and concentric rings (25), all of which reduce the number of excitations and thus the scan time compared to phase-encoded CSI. It is important to note that by explicitly encoding the spectral dimension, non-Cartesian trajectories that might normally be sensitive to off-resonance artifacts are rendered amenable to MRSI. All of these non-Cartesian rapid MRSI trajectories can be reconstructed using similar algorithms applied to non-Cartesian MRI such as gridding (26) or the non-uniform fast Fourier transform (nuFFT (27)).

However, the resulting speed advantage with EPSI comes at a cost of a coarser spectral resolution and limited spectral bandwidth ($SBW \approx 1/\Delta TE$), and also results in tradeoffs between spectral bandwidth, spatial resolution, and SNR efficiency (28). This tradeoff is compounded by the fact that the ^{13}C gyromagnetic ratio is roughly 1/4th that of ^{1}H, further increasing the demand on gradient strength and slew-rate and requiring the gradients to work four times as hard to achieve the same k-space coverage and ΔTE. This is particularly problematic at higher B_0 because the chemical shift difference (in Hz) between metabolites scales linearly with field strength, so that even higher bandwidths must be accommodated.

To increase the spectral bandwidth, rapid spectroscopic imaging *k*-space trajectories, including echo-planar, spiral and rings, can be interleaved by echo-shifting and/or rotating the trajectory, albeit at a cost of increased scan time. The tradeoff between several key parameters for different rapid MRSI strategies is summarized in Fig. 3.

Alternatively, accelerated spectroscopic imaging can also be performed with spatio-temporal encoding (SPEN), which has additional requirements of frequency swept excitation pulses whose effects are demodulated in the reconstruction. Inspired by multi-dimensional spectroscopy, SPEN utilizes a frequency-chirped RF excitation to impart a spatially dependent quadratic phase (29). Gradients applied during the readout shift the position of this localized point through physical space rather than k-space to construct an image (30). In SPEN, spatial information is recorded in the magnitude of the FID and spectral information is inherently recorded in its phase. This eliminates the need to explicitly encode spectral information using an EPSI-like readout.

Since the location of the sample is not encoded into the phase and de-mixed with a Fourier transform, like in conventional MRI, the SPEN technique is especially robust to B0 field inhomogeneities (31). SPEN has recently been extended to dynamic and multi-slice spectroscopic imaging of hyperpolarized compounds in both healthy rats and in a murine lymphoma model, showing good spatial agreement when compared to 2D CSI and good temporal agreement when compared to 1D dynamic spectra (32). With a temporal resolution on the order of 100 ms, SPEN will find utility when trying to acquire data with rapid reaction rates or where B0 homogeneity is poor.

The fast MRSI approaches form the backbone of several important pilot studies of hyperpolarized ^{13}C in cancer patients. This includes malignancies such as brain cancer (33,34), primary (35–37) and metastatic (38) prostate cancer, renal cell carcinoma (39) and pancreatic adenocarcinoma (40) (Fig. 4). The ability to cover a continuous chemical-shift spectrum allows resolution of downstream metabolic products without *a priori* knowledge of their identities or chemical shifts. Such chemical resolution is essential for pilot patient studies investigating new diseases or organs of interest, drug targets and metabolic pathway inhibition, or in the setting of HP probe development.

A potential limitation of fast spectroscopic imaging is the relatively long scan times versus imaging-based strategies, owing to the need to encode the spectral dimension. Such limitation can be partially offset by migrating to an imaging-based acquisition strategy (see the following section) in later phases of a clinical study where the ^{13}C substrate and products are assigned, and ΔB0/susceptibility has been better characterized for the target of interest. Having said this, the fast MRSI approaches still retain important application in those scenarios where quantitative accuracy and microenvironment characterization have priority over spatial coverage, for probe development when the metabolites aren’t yet known, or for when spatial localization is limited by the coil, such as prostate studies using an endorectal receive coil.

Model-based and Hybrid Spectroscopic Approaches

Model-based approaches can be combined with spectroscopic imaging to reduce the scan time in a hyperpolarized experiment. As with fast spectroscopic imaging, data are acquired at multiple echo times to jointly encode the spatial and spectral information. By taking advantage of prior knowledge, fewer echoes need to be acquired, accelerating the acquisition. HP ^{13}C spectra are amenable to model-based techniques because of the readily available prior knowledge of the number and relative chemical shift of ^{13}C resonances. The prior knowledge is then used to aid in the reconstruction of the undersampled data. In this section, we discuss two types of model-based reconstructions: Chemical Shift Encoding and the SPectroscopic Imaging by exploiting spatiospectral CorrElation (SPICE).

Chemical Shift Encoding

Chemical shift encoding methods, which include “Dixon” and IDEAL (Iterative Decomposition with Echo Asymmetry and Least squares estimation) (41), assume *a priori* knowledge of the substrates and products. For example, after injection of hyperpolarized [1-^{13}C]pyruvate, [1-^{13}C]pyruvate-hydrate and the metabolites [1-^{13}C]lactate, [1-^{13}C]alanine, and ^{13}C-bicarbonate can be observed (Fig. 1). Rather than having to satisfy the Nyquist sampling rate for accurate reconstruction, chemical shift encoding can reconstruct the expected resonances from far fewer echoes than would otherwise be possible.

For N different types of molecules, the signal at location r and echo time TE_m after excitation for Chemical Shift Encoding (CSE) is modeled as (42,43):

$$S_r\left(TE_m\right) = \left(\sum_{n=1}^{N} \rho_n\left(\sum_{j=1}^{J_n} q_{n,j} e^{i2\pi\Delta f_{n,j} TE_m}\right)\right)\exp\left(i2\pi\psi_r TE_m\right)$$

where TE_m is the m_{th} echo time, and Ψ_r is the off-resonance due to the main magnetic field at location r. For the molecule type indexed by n, there are J_n spectral peaks with Larmor frequencies $\Delta f_{n,j}$ and relative intensities $q_{n,j}$ such that $q_{n,1} + q_{n,2} + \ldots q_{n,j} = 1$ for all n. Note that ρ_n is a complex number for all n. The field map Ψ can be determined from ^{1}H data and scaled to the ^{13}C frequency. The matrix inversion can occur in either k-space (43–45) or image-space (42) to extract images for each metabolite of interest (Fig. 5).

Model-based approaches have been used pre-clinically in the study of kidney (46,47), cardiac (48), and tumor metabolism (43,49), and in healthy volunteers (50) to characterize brain metabolism. The advantage with chemical shift encoding is that only N echoes are required to solve the system given the measured ^{1}H field map, reducing the total scan time compared to encoding the full spectrum with MRSI. However, the echo spacing needs to be carefully chosen to avoid noise amplification in the matrix inversion. This can be optimized by calculating the effective number of signal averages (NSA) for each ^{13}C metabolite (42), which is a measure of relative SNR for each metabolite and is a function of chemical shift and sampled echo-times. Choosing an optimal echo spacing becomes more difficult when many resonances are present, or when spectral peaks are poorly separated. Frequency swaps

can also occur if the B0 field map is unaccounted for or if it changes during the acquisition, potentially leading to quantification errors and introducing artifacts.

SPectroscopic Imaging by exploiting spatiospectral CorrElation (SPICE)

An alternative model-based method is SPectroscopic Imaging by exploiting spatiospectral CorrElation (SPICE). SPICE is a combined data acquisition protocol and image reconstruction algorithm that exploits the partial separability inherent to spectroscopic signals (51,52) to reconstruct high-resolution spectroscopic imagery. SPICE is comprised of two separate data collections: one is of low-spatial and high-temporal resolution (i.e. high spectral bandwidth), while the other is of high-spatial and low-temporal resolution (53). The data acquisition protocol is depicted in Fig. 6. The first acquisition is a phase-encoded CSI sequence used to estimate the spectral signatures of the molecules in the imaged sample. The reconstructed imagery is constrained so that each voxel generates a linear combination of these signatures. The second sequence is an EPSI sequence, used to attain a sparse sampling of high spatial-resolution data.

From the CSI acquisition, a two-dimensional spatial Fourier transform reconstructs a high-temporal but low-spatial resolution dataset. It is assumed that each voxel is comprised of a small number of different molecules. In this case, the temporal signal exhibited by any voxel can be expressed as

$$\rho\left(r,t\right)=\sum_{j=1}^{J(r)}c_j(r)\varphi_j(t)$$

where φ_j is the temporal signal exhibited by molecule j and c_j is the amount of molecule j at location r. By exploiting the partial separability of this model, the individual spectral signatures are identified (51,52). SPICE next reconstructs high-resolution imagery by constraining the output of each voxel to be a linear combination of the known signals. SPICE reconstructs the high-resolution spectroscopic imagery by solving the follow optimization problem

$$\text{minimize}\left(\frac{1}{2}\right)\|DF_B\Phi\|_{Fr}^2+\lambda\Psi\left(\Phi C\right)$$

where $\|\cdot\|_{\text{Fr}}$ represents the Frobenius norm, F_B is a transformation that performs a Discrete Fourier Transform and removes off-resonance due to B_0 field inhomogeneity, Φ is a matrix of the spectral signatures, Ψ is a regularization function and $\lambda \geq 0$ is a regularization parameter. In (54), Lam et al. set $\Psi(\Phi C) = \|DC\Phi\|_{W,\text{Fr}}$ where $\|\cdot\|_{W,\text{Fr}}$ is a weighted Frobenius norm with weights W and D is a finite difference operator. This yields a least-squares problem, which can be solved with known algorithms (55).

While SPICE has been used extensively in ^{1}H MRSI (56–58), it has only recently been applied to hyperpolarized ^{13}C applications. Lee et al (53) applied SPICE at 9.4 T to create spectroscopic images of mouse kidneys at high-resolution (0.47 × 0.47 mm^2) for a single timepoint, showing that SPICE reconstruction outperformed a standard EPSI approach. In

(59), Song et al. extended SPICE to a single-slice dynamic acquisition. The calibration dataset was acquired once, but 10 separate high-spatial resolution datasets were acquired every 2 s, with a reconstructed spatial resolution up to $1 \times 1mm^2$. An important constraint to the dynamic SPICE scheme is choosing an appropriate scan timing for D1 in order to derive a complete basis of substrate and products. This may offset the subsequent D2 timing, missing the initial pyruvate-to-lactate dynamics and therefore deteriorating quantitative accuracy of disease metabolism.

Metabolite-Specific Imaging

Fast spectroscopic imaging and model-based imaging approaches acquire spectral and spatial information simultaneously, decoupling multiple metabolite signals using multi-echo readouts. Alternatively, metabolite-specific imaging uses a specialized RF pulse and a rapid imaging readout to encode the spectral and spatial domains in two distinct steps. In this approach, a singleband spectral-spatial RF pulse that is both frequency- and slice-selective performs the spectral encoding, exciting a single metabolite within a slice (or slab) (60). A rapid imaging readout trajectory, typically single-shot echoplanar (61,62) or spiral (63), is then used to spatially encode the magnetization as a 2D multi-slice or 3D slab encoded dataset. The acquisition then cycles through the resonances of interest over time to acquire a volumetric dynamic dataset for each metabolite (Fig. 7). An example of metabolite-specific EPI can be seen in Fig. 8, showing pyruvate uptake and conversion to lactate and bicarbonate throughout the brain at a spatial resolution of $1.5 \times 1.5 \times 2.0\ cm^3$ (64). These total signal (area under the curve) images show that artifact-free data can be acquired with rapid imaging readouts in the clinical setting, enabling volumetric coverage of the whole brain with a temporal resolution (3 s in this study) equivalent to that of single slice EPSI. This type of approach is inherently more flexible than spectroscopic imaging or model-based sequences, as the metabolites of interest can be selectively excited and encoded, eliminating the need to encode the entire spectrum. The total acquisition time can also be significantly reduced if single-shot readouts are employed, greatly reducing the scan time and making the acquisition more robust to motion compared to a MRSI acquisition.

However, metabolite specific imaging requires a sparse spectrum with well-separated resonances, which is dependent on the chemical shift of metabolites and the operating field strength. This approach is therefore not applicable to all substrates but is well suited to imaging of [1-^{13}C]pyruvate (Fig. 1) since all five resonances are separated by at least 3 ppm, or 93 Hz at 3T. Because each metabolite is excited and encoded separately, optimized flip angle strategies that provide metabolite-specific flip angles can be easily integrated, which have been shown to increase SNR over a constant flip angle scheme (65,66).

The rapid imaging readouts used in metabolite-specific imaging are also more sensitive to center frequency errors and B0 field inhomogeneity when compared to spectroscopic or model-based approaches. This will manifest as geometric distortion or blurring in metabolite data acquired with echoplanar and spiral readouts, respectively, due to the accumulation of phase during the readout. These artifacts can be partially mitigated by shortening the readout duration, albeit at the cost of reduced SNR efficiency. They can also be reduced through off-resonance and distortion correction strategies developed for ^{1}H MRI that are also compatible

with hyperpolarized ^{13}C MRI. For spiral, auto-focus algorithms (67) have been used to correct for B0-induced blurring. For EPI, an alternating blip strategy (68) or integrated dual-echo readout (69) can be used to estimate and correct for B0 distortion. Symmetric echoplanar readouts additionally can suffer from Nyquist ghost artifacts due to inconsistencies between the phase encodings, which can be corrected for by estimating the phase coefficients from a ^{1}H reference scan using the ^{13}C waveform (62) or via an exhaustive search (70).

Because the RF pulse performs the spectral encoding, proper frequency calibration is crucial. Miscalibration of the center frequency and the B0 field inhomogeneity will reduce the applied flip angle due to the narrow passband of the SPSP RF pulse (typically ±2.5ppm FWHM for [1-^{13}C]pyruvate applications). The reduced flip angle will lead to overall reduced SNR and can potentially bias quantification if left unaccounted.

The remaining sections will focus on additional pulse sequence options that are compatible with the acquisition methods discussed above. These sequence options can be used to improve scan coverage, speed, SNR, resolution, and/or robustness in a hyperpolarized experiment.

Refocused Imaging Methods

Because of the non-renewable magnetization, the imaging methods discussed in the previous sections are all typically acquired as gradient echo sequences, where transverse magnetization is spoiled at the end of each TR. A potentially more efficient way to use nonrenewable hyperpolarized signals is to repetitively refocus transverse spins, which is especially valuable for imaging metabolites with long T2s such as [1-^{13}C]pyruvate, [1-^{13}C]lactate and [^{13}C, $^{15}N_2$] urea (71–75). Two types of sequences have been explored for spin refocusing of hyperpolarized substrates: the balanced steady state free precession (“bSSFP”) sequence and the fast spin echo (“FSE”) sequence.

Balanced SSFP (bSSFP) sequences

In the bSSFP sequence, a train of refocusing pulses with angle θ is applied with alternating polarity and net gradient areas that are always zero between two neighboring refocusing pulses. Typically, each bSSFP timepoint is preceded by a θ/2 preparation pulse TR/2 before the first imaging repetition to reduce transient state oscillations, and is ended by a θ/2 tip back pulse to return magnetization to the longitudinal axis (76). The θ/2 preparation pulse can be replaced by a set of linear ramped preparation pulses to improve its robustness to off-resonance frequencies and power variations (77).

The bSSFP sequence has an intrinsic periodic frequency response (Fig. 9A) at repetitions of 1/TR. The choice of flip angle of the excitation passband in the bSSFP sequence is a tradeoff between alleviating banding artifacts and preserving magnetization for dynamic imaging. A large flip angle (>100°) is favorable to reduce banding artifacts but limits the total available scan time because the majority of the magnetization is tipped into the transverse plane, leading to signal decay via T2 rather than T1 relaxation. However, to perform dynamic imaging in hyperpolarized studies, a small flip angle is necessary to preserve sufficient

magnetization for subsequent time points. An intermediate flip angle (e.g. 60°) can be used to achieve a compromise between the two factors. In addition to TR and flip angle, the spectral response of the RF excitation profile can also influence the bSSFP signal (74) and must also be taken into consideration to avoid off-resonance excitation.

Three bSSFP strategies have been used in hyperpolarized ^{13}C studies (Fig. 9B–D). The first strategy (Fig. 9B) utilized a broadband pulse to excite all metabolites and reconstructed the spectral information from multi-echo readouts using chemical shift encoding (71) or fitting of multiple acquisitions with variable phase advance (78). This strategy is advantageous to acquire all metabolites at the same time, but it requires long TRs and limits the optimization of scan parameters (e.g. flip angle, resolution) for individual compounds.

The second strategy (Fig. 9C) excites one metabolite at a time and has been applied for imaging metabolically inert agents with a single HP resonance such as urea (8,73,75,76,79–81), or imaging multiple metabolites at ultra-high field (e.g. 14.1 T) (74,82) (Fig. 10). At ultra-high fields, frequency separation between metabolites is sufficiently large to enable spectrally selective RF pulses short enough to meet the short TR constraint in the bSSFP sequence. However, adapting this strategy to clinical field-strength at 1.5T or 3T is challenging due to the long RF pulses needed to obtain spectral selectivity.

The third strategy (Fig. 9D) extends metabolite specific imaging with bSSFP to lower field, where the frequency separation between metabolites can hamper spectral selectivity, by using a chemical saturation pulse to suppress undesired signals at the beginning of each timepoint (72). This strategy alleviates the constraint of RF pulse duration. However, the pre-saturated signal may replenish due to inflow or metabolism and contaminate later data, and saturation performance also heavily depends on a homogeneous transmit B1 profile.

Fast Spin-echo (FSE) sequences

Fast spin echo (FSE) sequences, also known as turbo spin-echo (TSE) or rapid acquisition with refocused echoes (RARE), typically use 180° refocusing pulses surrounded by a pair of identical crusher gradients. Compared with bSSFP sequences, FSE sequences are substantially less sensitive to B0 inhomogeneity, and have no constraint of short TR which allows a longer RF excitation pulse to achieve a better metabolite selection. Refocusing pulse design can be either Shinnar-Le Roux (SLR) pulses or adiabatic inversion pulses.

SLR pulses are sensitive to B1 variation and thus susceptible to imperfect refocusing and loss of nonrenewable hyperpolarization, making them most suitable for single time point imaging. Sukumar et. al. (83) utilized a 3D FSE sequence with a 180-degree SLR pulse and EPI readouts to acquire 3D volumes from a single timepoint in co-polarized studies with [1-^{13}C]pyruvate and [^{13}C]urea at 14.1 T. Yen et al. (84) has applied a non-CPMG (77) echo train with SLR refocusing pulses to improve the realignment of longitudinal magnetization as well as keep the transverse magnetization refocused.

Compared with SLR pulses, adiabatic pulses are insensitive to B1 above the adiabatic threshold, which is crucial to preserve hyperpolarized magnetization. However, under the constraint of specific absorption rate (SAR) limit, the high RF power of adiabatic pulses

limits the density of these pulses, making it challenging for clinical translation. Wang et al. has developed a 3D FSE sequence using adiabatic pulses and stack of spiral readouts on a pre-clinical 7T system, with data acquisition either at only even echoes (85) or at all echoes (86). In a later work (86), the authors found the quadratic phase variation of transverse magnetization to be small (<0.02 rad) over a small range (±50 Hz) of frequency variation, and thus signals can be acquired at echoes formed by unpaired adiabatic pulses. However, the phase and magnitude profile of unpaired adiabatic pulses were not analyzed as a function of RF power, and phase mismatch between odd and even echoes could occur as a function of B1 and lead to aliasing artifacts. Spatial B1 inhomogeneity will also result in phase inconsistency across voxels, complicating the reconstruction. Therefore, the utility of signals at echoes formed by unpaired adiabatic pulses needs to be further evaluated.

Calibration Methods

Accurate RF calibration and variations in bolus timing between subjects presents significant challenges to acquiring robust and reproducible hyperpolarized datasets. Center frequency and RF power calibration is crucial to the success of all imaging approaches but is difficult to perform due to the lack of endogenous ^{13}C signal. One common strategy is to perform this calibration on an external ^{13}C-enriched phantom (37,50,64). However, this approach does not fully account for the variability between subjects, or for variation in the B1+ field of surface coils. Susceptibility variations of tissues will contribute to spatial B0 inhomogeneity while subject loading causes a bulk RF power offset. As an alternative, center frequency calibration can be performed based on the measured water ^{1}H frequency and then converted to the ^{13}C operation frequency after accounting for differences in chemical shift (87).

Appropriate acquisition timing for hyperpolarized ^{13}C imaging is also important to avoid saturation of the nonrecoverable hyperpolarized spins during bolus arrival, particularly near the transmitter conductive elements where the $B1^{+}$is high. Many variable flip angle schemes (88–91) also assume knowledge of the bolus shape and timing, but variability in bolus kinetics leads to quantification errors in the context of ratiometric measures (92,93). A fixed delay between injection and acquisition have been employed in many hyperpolarized ^{13}C imaging studies (34,35,50,63) but the empirically determined delay time can be unreliable due to the inherent physiological variability between subjects, and in human cancers where the vascularization and perfusion are highly variable over subjects (94). This is particularly problematic in human subjects in which timing differences of up to 12 s have been observed in hyperpolarized ^{13}C studies of prostate cancer patients (35,36).

Variable perfusion characteristics can be resolved using a bolus tracking technique to trigger the acquisition upon pyruvate arrival, as demonstrated in work by Durst et al (92) and Tang et al (95). Center frequency and RF power calibration using a Bloch-Siegert approach can also be incorporated into bolus tracking (95), eliminating the challenges associated with RF calibration and variations in bolus timing. The primary disadvantage of using a real-time bolus tracking framework is the engineering efforts to address system compatibility issue and the potentially complicated analysis of bolus kinetics.

Tailored Flip Angles

In hyperpolarized metabolic imaging, the flip angles must be chosen carefully to efficiently utilize magnetization before the irreversible signal decay to thermal equilibrium and to measure the dynamic metabolic conversion occurring during the experiment. The irreversible signal decay occurs both due to T_1 relaxation and RF excitation. This limits the overall duration of the hyperpolarized experiment as well as the number of measurements that can be made. In order to observe metabolic conversion to downstream metabolites, which are typically SNR-limited, care must be taken to not saturate the magnetization of the injected metabolite substrate.

There are two main strategies used to choose the flip angles for hyperpolarized metabolic imaging experiments: variable flip angles, in which the flip angles are changed throughout the acquisition, and metabolite-specific flip angles, in which the flip angle is varied across metabolites. Variable flip angle schemes take into account the effect of prior RF pulses throughout the acquisition to efficiently use the hyperpolarized magnetization, regardless of whether these are used to encode a single image or across time points. In a single image that requires multiple excitations, using constant flip angles will result in varying signal amplitudes, leading to k-space modulations that can create blurring or other artifacts depending on the phase-encoding scheme used (96). Variable flip angle schedules that account for prior RF pulses can be used to eliminate this modulation, theoretically providing constant signal amplitudes across excitations. When acquiring multiple time points to measure the conversion kinetics, variable flip angles can be designed to maximize total SNR or improve estimates of conversion rates (91). The main challenge using variable flip angles is that they are more sensitive to the timing of the acquisition relative to the bolus characteristics and to inhomogeneities in the transmit B1 field (97). Thus they will work best when paired with advanced calibration methods described above.

Metabolite-specific flip angles aim to preserve the magnetization of the hyperpolarized substrate and improve the SNR of the downstream metabolic products (65,66) (Fig. 11). This is feasible because the injected substrate (e.g. pyruvate) is typically present at a much higher concentration, and thus the flip angle can be reduced while still maintaining adequate substrate SNR. Meanwhile, reducing the substrate flip angle preserves more of this magnetization for metabolic conversion, and downstream products can be excited with a higher flip angle to improve their SNR. The implementation of this strategy is straightforward in metabolite-specific imaging since only one metabolite is excited at a time. Multiband spectral-spatial RF pulses can be designed to modulate the flip angle across metabolites in spectroscopic or hybrid methods, albeit within the constraints of the RF pulse design algorithm (65).

When using tailored flip angles, it is important to include these effects in the data analysis. This is made more challenging by the fact that each excitation, particularly those on the substrate, affects all downstream metabolite measurements as well as later time points. In kinetic modeling, arbitrary flip angle and acquisition timings can be incorporated using a hybrid discrete-continuous model (91,93,97,98).

Another often neglected consideration are slice profile effects (99). These arise from the imperfect excitation profile of slice-selective RF pulses. Cumulative RF effects in the transition regions of slice-selective RF pulses, where the flip angles are less than expected, leads to excess signal after repeated excitations. This is especially pronounced later in the acquisition or when larger flip angles are used, potentially leading to quantification errors if unaccounted for. Several simple solutions include using smaller flip angles or performing 3D encoding. More complex solutions include using gradient scaling or redesigned RF pulses (100,101) and models that simulate all locations across the slice (91).

Acceleration Strategies

Because of the limited lifetime of hyperpolarized substrates, reducing the total scan time and increasing temporal resolution can improve SNR and image quality. Both parallel imaging and compressed-sensing are applicable to hyperpolarized ^{13}C MRI and can be applied to the aforementioned imaging sequences discussed above.

Parallel imaging can be used to improve volumetric coverage and/or reduce the scan time in hyperpolarized experiments that utilize multichannel arrays. The undersampled data can be reconstructed either in the image domain using known coil sensitivities or in the spatial frequency domain from auto calibrating signals in the fully sampled center of k-space. Because of the limited magnetization, coil sensitivities are typically not directly measured with the hyperpolarized substrate. Instead, the sensitivity maps can be estimated via numerical simulation (102), from a separate pre-calibration scan using a thermal (non-hyperpolarized) ^{13}C phantom (103), or they can be estimated from the fully-sampled central region of k-space (104,105). Calibrationless parallel imaging approaches (such as SAKE (106)) are also well-suited for hyperpolarized substrates, as they eliminate the need to explicitly estimate coil sensitivity maps or acquire a fully-sampled center of k-space. Calibrationless parallel imaging has been used in conjunction with a fourfold undersampled 3D EPI acquisition to acquire cardiac and renal metabolic data in a single volumetric acquisition in a healthy human volunteer study using [1-^{13}C]pyruvate (107). A simultaneous multi-slice acquisition with 2-fold acceleration and a large 48 × 48 × 24 cm^3 FOV has also been successfully demonstrated for hyperpolarized ^{13}C imaging experiments using pigs (108). However, it is important to note that parallel imaging can still reduce the overall SNR in a hyperpolarized experiment. While the acceleration penalty (√R) can be offset by increasing the flip angle to compensate for fewer RF excitations, g-factor noise amplification will still be present and will lead to an SNR penalty dependent on both the coil geometry (109) and sampling pattern (25).

Acceleration can also be achieved through compressed sensing (110) and is particularly useful when multichannel arrays are not used. HP ^{13}C MRI is particularly amenable for compressed sensing because it is typically not limited by SNR but rather by encoding time, and the resulting spectra are typically sparse. Compressed sensing has been utilized in echoplanar spectroscopic imaging for human acquisitions using pseudo-random blip gradients that are applied during an EPSI readout and constraining the reconstruction based on sparsity in the spectral and dynamic imaging dimensions to achieve 3D MRSI with 2 s temporal resolution (37,111,112). To overcome the bandwidth limitations of EPSI, blip

gradients can be applied during the readout in phase-encoded 2D MRSI for both acceleration and high-bandwidth applications (113). Compressed sensing has been demonstrated in 2D metabolic imaging of the rat heart using a single-shot echoplanar readout at a spatial resolution of $1\times1\times3.5$ mm^3 with up to 5-fold acceleration (114), and in rat kidneys with a 3D EPI sequence using a psueudorandom blip scheme in the z-dimension, achieving up to 3-fold acceleration (115). Compressed sensing can also be in conjunction with model-based approaches to further accelerate the acquisition (46,114). However, choosing the proper value for the regularization parameter λ requires numerical simulations or empirical studies to determine the tradeoff between data consistency and excessive de-noising, which can impact quantification if not properly tuned.

Future Outlook

The current state-of-the-art for fast hyperpolarized metabolic imaging includes rapid spectroscopic imaging, model-based methods, and metabolite-specific imaging, which are summarized in terms of pros and cons in Table 1, as well as tradeoffs in terms of flexibility of acquisition, speed, robustness to field inhomogeneities, ability to capture complex spectral, and compatibility with acceleration methods in Fig. 2. The speed, SNR and/or robustness of all of these approaches can be improved by the addition of parallel imaging, compressed sensing, tailored flip angle schemes, refocused imaging methods, and real-time calibrations. The pros and cons of these various sequence options are summarized in Table 2.

Our experience is that metabolite-specific imaging provides the best performance in terms of speed, coverage, and acquisition flexibility for human studies with [1-^{13}C]pyruvate, the most widely used hyperpolarized ^{13}C agent. The main failure mode of this approach is B0 inhomogeneities, which has not been a major issue and is mitigated through ^{1}H-based shimming prior to ^{13}C studies. We have been using metabolite-specific flip angles, with lower flip angles on pyruvate and higher flip angles for the metabolic products, to improve the overall SNR. While we have used variable flip angles in past studies, we are not including them in current studies due to their sensitivity to transmit B1+ inhomogeneities and calibration errors, both of which have proven to be a limitation with current ^{13}C hardware. We have also been increasingly incorporating real-time calibrations of bolus timing, B_0, and B_1^+ to improve the reproducibility and SNR, and they also will facilitate future use of variable flip angles to improve SNR and quantification.

Looking forward, we anticipate fast imaging improvements for other hyperpolarized agents, increasing spatial coverage, and improving SNR and/or resolution. For clinical applications of hyperpolarized agents beyond [1-^{13}C]pyruvate (21) or combinations of multiple agents, metabolite-specific imaging may no longer be an option due to increased spectral complexity and reduced spectral separation. For these studies, we anticipate improved model-based approaches will provide fast imaging techniques. Future human studies will also likely have increased demands on spatial coverage (e.g. for metastatic disease), which will require use of parallel imaging and/or compressed sensing for acceleration. Refocused imaging offers incredible potential for improving the resolution and SNR of hyperpolarized studies several fold due to the long T_2 relaxation times (75,116). We are optimistic that these

approaches will develop the selectivity and robustness needed for future human imaging studies.

In summary, current techniques for fast hyperpolarized metabolic imaging can provide rapid, volumetric, and dynamic imaging of metabolic conversion in human studies. These techniques will most certainly improve in terms of SNR, resolution, coverage, and reproducibility with additional hardware, pulse sequence, and reconstruction developments.

Acknowledgements:

We would like to acknowledge the UCSF Hyperpolarized Technology Resource Center (HMTRC) led by Prof. Dan Vigneron (NIH P41 EB013598), as well as NIH grants R01CA211150, U01CA232320, U01EB026412, UCSF Quantitative Bioscience Institute Postdoctoral Fellowship, and American Cancer Society Research Scholar Grant RSG-18-005-01-CCE.

References

1. Kurhanewicz J, Vigneron DB, Brindle K, Chekmenev EY, Comment A, Cunningham CH, DeBerardinis RJ, Green GG, Leach MO, Rajan SS, Rizi RR, Ross BD, Warren WS, Malloy CR. Analysis of Cancer Metabolism by Imaging Hyperpolarized Nuclei: Prospects for Translation to Clinical Research. Neoplasia 2011;13(2):81–97. [PubMed: 21403835]
2. Vander Heiden MG, Cantley LC, Thompson CB. Understanding the Warburg Effect: The Metabolic Requirements of Cell Proliferation. Science 2009;324(5930):1029–1033. [PubMed: 19460998]
3. Guglielmetti C, Chou A, Krukowski K, Najac C, Feng X, Riparip L-K, Rosi S, Chaumeil MM. In vivo metabolic imaging of Traumatic Brain Injury. Scientific Reports 2017;7(1):17525. [PubMed: 29235509]
4. DeVience SJ, Lu X, Proctor J, Rangghran P, Melhem ER, Gullapalli R, Fiskum GM, Mayer D. Metabolic imaging of energy metabolism in traumatic brain injury using hyperpolarized [1-(13)C]pyruvate. Scientific reports 2017;7(1):1907–1907. [PubMed: 28507314]
5. Guglielmetti C, Najac C, Didonna A, Van der Linden A, Ronen SM, Chaumeil MM. Hyperpolarized 13C MR metabolic imaging can detect neuroinflammation in vivo in a multiple sclerosis murine model. Proceedings of the National Academy of Sciences 2017;114(33):E6982.
6. Moon C-M, Shin S-S, Lim N-Y, Kim S-K, Kang Y-J, Kim H-O, Lee S-J, Beak B-H, Kim Y-H, Jeong G-W. Metabolic alterations in a rat model of hepatic ischaemia reperfusion injury: In vivo hyperpolarized 13C MRS and metabolic imaging. Liver International 2018;38(6):1117–1127. [PubMed: 29345050]
7. Laustsen C, Østergaard JA, Lauritzen MH, Nørregaard R, Bowen S, Søgaard LV, Flyvbjerg A, Pedersen M, Ardenkjær-Larsen JH. Assessment of early diabetic renal changes with hyperpolarized [1–13C]pyruvate. Diabetes/Metabolism Research and Reviews 2013;29(2):125–129. [PubMed: 23166087]
8. von Morze C, Larson PEZ, Hu S, Keshari K, Wilson DM, Ardenkjaer-Larsen JH, Goga A, Bok R, Kurhanewicz J, Vigneron DB. Imaging of blood flow using hyperpolarized [13C]Urea in preclinical cancer models. Journal of Magnetic Resonance Imaging 2011;33(3):692–697. [PubMed: 21563254]
9. Lau AZ, Miller JJ, Robson MD, Tyler DJ. Cardiac perfusion imaging using hyperpolarized 13c urea using flow sensitizing gradients. Magnetic Resonance in Medicine 2016;75:1474–1483. [PubMed: 25991580]
10. Gallagher FA, Kettunen MI, Hu D-E, Jensen PR, Zandt Rit, Jensen M, Gisselsson A, Nelson SK, Witney TH, Bohndiek SE, Hansson PR, Peitersen G, Lerche MH, Brindle KM. Production of hyperpolarized [1,4–13C2]malate from [1,4–13C2]fumarate is a marker of cell necrosis and treatment response in tumors. Proceedings of the National Academy of Sciences 2009;106(47):19801–19806.
11. Chaumeil MM, Larson PEZ, Yoshihara HAI, Danforth OM, Vigneron DB, Nelson SJ, Pieper RO, Phillips JJ, Ronen SM. Non-invasive in vivo assessment of IDH1 mutational status in glioma. Nat Commun 2013;4.

12. Gallagher FA, Kettunen MI, Day SE, Hu DE, Ardenkjaer-Larsen JH, Zandt R, Jensen PR, Karlsson M, Golman K, Lerche MH, Brindle KM. Magnetic resonance imaging of pH in vivo using hyperpolarized 13C-labelled bicarbonate. Nature 2008;453(7197):940–943. [PubMed: 18509335]
13. Ball DR, Rowlands B, Dodd MS, Le Page L, Ball V, Carr CA, Clarke K, Tyler DJ. Hyperpolarized butyrate: A metabolic probe of short chain fatty acid metabolism in the heart. Magnetic Resonance in Medicine 2014;71:1663–1669. [PubMed: 23798473]
14. Keshari KR, Kurhanewicz J, Bok R, Larson PEZ, Vigneron DB, Wilson DM. Hyperpolarized 13C dehydroascorbate as an endogenous redox sensor for in vivo metabolic imaging. Proceedings of the National Academy of Sciences 2011;108(46):18606–18611.
15. Keshari KR, Wilson DM. Chemistry and biochemistry of 13C hyperpolarized magnetic resonance using dynamic nuclear polarization. Chemical Society Reviews 2014;43(5):1627–1659. [PubMed: 24363044]
16. Ardenkjær-Larsen JH, Fridlund B, Gram A, Hansson G, Hansson L, Lerche MH, Servin R, Thaning M, Golman K. Increase in signal-to-noise ratio of > 10,000 times in liquid-state NMR. Proc Natl Acad Sci USA 2003;100(18):10158–10163. [PubMed: 12930897]
17. Kovtunov KV, Pokochueva EV, Salnikov OG, Cousin SF, Kurzbach D, Vuichoud B, Jannin S, Chekmenev EY, Goodson BM, Barskiy DA, Koptyug IV. Hyperpolarized NMR Spectroscopy: d-DNP, PHIP, and SABRE Techniques. Chemistry – An Asian Journal 2018;13(15):1857–1871.
18. Adams RW, Aguilar JA, Atkinson KD, Cowley MJ, Elliott PIP, Duckett SB, Green GGR, Khazal IG, López-Serrano J, Williamson DC. Reversible Interactions with para-Hydrogen Enhance NMR Sensitivity by Polarization Transfer. Science 2009;323(5922):1708. [PubMed: 19325111]
19. Kohler SJ, Yen Y, Wolber J, Chen AP, Albers MJ, Bok R, Zhang V, Tropp J, Nelson S, Vigneron DB, Kurhanewicz J, Hurd RE. In vivo 13carbon metabolic imaging at 3T with hyperpolarized 13C-1-pyruvate. Magnetic Resonance in Medicine 2007;58(1):65–69. [PubMed: 17659629]
20. Golman K, in ‘t Zandt R, Thaning M. Real-time metabolic imaging. Proceedings of the National Academy of Sciences 2006;103(30):11270.
21. Chung BT, Chen H-Y, Gordon J, Mammoli D, Sriram R, Autry AW, Le Page LM, Chaumeil M, Shin P, Slater J, Tan CT, Suszczynski C, Chang S, Li Y, Bok RA, Ronen SM, Larson PEZ, Kurhanewicz J, Vigneron DB. First hyperpolarized [2–13C]pyruvate MR studies of human brain metabolism. Journal of Magnetic Resonance 2019;309:106617. [PubMed: 31648132]
22. Yen Y-F, Kohler SJ, Chen AP, Tropp J, Bok R, Wolber J, Albers MJ, Gram KA, Zierhut ML, Park I, Zhang V, Hu S, Nelson SJ, Vigneron DB, Kurhanewicz J, Dirven HAAM, Hurd RE. Imaging considerations for in vivo 13C metabolic mapping using hyperpolarized 13C-pyruvate. Magn Reson Med 2009;62(1):1–10. [PubMed: 19319902]
23. Mayer D, Levin YS, Hurd RE, Glover GH, Spielman DM. Fast metabolic imaging of systems with sparse spectra: application for hyperpolarized 13C imaging. Magn Reson Med 2006;56(4):932–937. [PubMed: 16941617]
24. Ramirez MS, Lee J, Walker CM, Sandulache VC, Hennel F, Lai SY, Bankson JA. Radial spectroscopic MRI of hyperpolarized [1-(13) C] pyruvate at 7 tesla. Magn Reson Med 2013.
25. Jiang W, Lustig M, Larson PEZ. Concentric rings K-space trajectory for hyperpolarized (13) C MR spectroscopic imaging. Magn Reson Med 2014.
26. Jackson JI, Meyer CH, Nishimura DG, Macovski A. Selection of a Convolution Function for Fourier Inversion Using Gridding. IEEE Trans Med Imaging 1991;10(3):473–478. [PubMed: 18222850]
27. Fessler JA, Sutton BP. Nonuniform fast Fourier transforms using min-max interpolation. IEEE Trans Signal Proc 2003;51(2):560–574.
28. Yen YF, Kohler SJ, Chen AP, Tropp J, Bok R, Wolber J, Albers MJ, Gram KA, Zierhut ML, Park I, Zhang V, Hu S, Nelson SJ, Vigneron DB, Kurhanewicz J, Dirven HAAM, Hurd RE. Imaging considerations for in vivo 13C metabolic mapping using hyperpolarized 13C-pyruvate. Magnetic Resonance in Medicine 2009;62(1):1–10. [PubMed: 19319902]
29. Ben-Eliezer N, Irani M, Frydman L. Super-resolved spatially encoded single-scan 2D MRI. Magnetic Resonance in Medicine 2010;63(6):1594–1600. [PubMed: 20512863]
30. Tal A, Frydman L. Single-scan multidimensional magnetic resonance. Progress in Nuclear Magnetic Resonance Spectroscopy 2010;57(3):241–292. [PubMed: 20667401]

31. Zhang Z, Lustig M, Frydman L. Phase-encoded xSPEN: A novel high-resolution volumetric alternative to RARE MRI. Magnetic Resonance in Medicine 2018;80(4):1492–1506. [PubMed: 29498093]
32. Schmidt R, Laustsen C, Dumez J-N, Kettunen MI, Serrao EM, Marco-Rius I, Brindle KM, Ardenkjaer-Larsen JH, Frydman L. In vivo single-shot 13C spectroscopic imaging of hyperpolarized metabolites by spatiotemporal encoding. Journal of Magnetic Resonance 2014;240:8–15. [PubMed: 24486720]
33. Park I, Larson PEZ, Gordon JW, Carvajal L, Chen HY, Bok R, Van Criekinge M, Ferrone M, Slater JB, Xu D, Kurhanewicz J, Vigneron DB, Chang S, Nelson SJ. Development of methods and feasibility of using hyperpolarized carbon-13 imaging data for evaluating brain metabolism in patient studies. Magnetic Resonance in Medicine 2018;80(3):864–873. [PubMed: 29322616]
34. Miloushev VZ, Granlund KL, Boltyanskiy R, Lyashchenko SK, DeAngelis LM, Mellinghoff IK, Brennan CW, Tabar V, Yang TJ, Holodny AI, Sosa RE, Guo YW, Chen AP, Tropp J, Robb F, Keshari KR. Metabolic Imaging of the Human Brain with Hyperpolarized 13C Pyruvate Demonstrates 13C Lactate Production in Brain Tumor Patients. Cancer Research 2018;78(14):3755. [PubMed: 29769199]
35. Nelson SJ, Kurhanewicz J, Vigneron DB, Larson PEZ, Harzstark AL, Ferrone M, van Criekinge M, Chang JW, Bok R, Park I, Reed G, Carvajal L, Small EJ, Munster P, Weinberg VK, Ardenkjaer-Larsen JH, Chen AP, Hurd RE, Odegardstuen L-I, Robb FJ, Tropp J, Murray JA. Metabolic Imaging of Patients with Prostate Cancer Using Hyperpolarized [1–13C]Pyruvate. Science Translational Medicine 2013;5(198):198ra108.
36. Granlund KL, Tee S-S, Vargas HA, Lyashchenko SK, Reznik E, Fine S, Laudone V, Eastham JA, Touijer KA, Reuter VE, Gonen M, Sosa RE, Nicholson D, Guo YW, Chen AP, Tropp J, Robb F, Hricak H, Keshari KR. Hyperpolarized MRI of Human Prostate Cancer Reveals Increased Lactate with Tumor Grade Driven by Monocarboxylate Transporter 1. Cell Metabolism 2019.
37. Chen H-Y, Larson PEZ, Gordon JW, Bok RA, Ferrone M, Criekinge M, Carvajal L, Cao P, Pauly JM, Kerr AB, Park I, Slater JB, Nelson SJ, Munster PN, Aggarwal R, Kurhanewicz J, Vigneron DB. Technique development of 3D dynamic CS-EPSI for hyperpolarized 13C pyruvate MR molecular imaging of human prostate cancer. Magnetic Resonance in Medicine 2018;80(5):2062–2072. [PubMed: 29575178]
38. Chen H, Aggarwal R, Bok R, Ohliger M, Zhu Z, Lee P, Gordon Jeremy W, Criekinge MV, Carvajal L, Slater James B, Larson Peder EZ, Small EJ, Kurhanewicz J, Vignaud A. Hyperpolarized 13C-Pyruvate MRI Detects Real-Time Metabolic Flux in Prostate Cancer Metastases to Bone and Liver: A Clinical Feasibility Study. Prostate Cancer and Prostatic Diseases 2019 (In Press). 10.1038/s41391-019-0180-z.
39. Tran M, Latifoltojar A, Neves JB, Papoutsaki M-V, Gong F, Comment A, Costa ASH, Glaser M, Tran-Dang M-A, El Sheikh S, Piga W, Bainbridge A, Barnes A, Young T, Jeraj H, Awais R, Adeleke S, Holt C, O'Callaghan J, Twyman F, Atkinson D, Frezza C, Årstad E, Gadian D, Emberton M, Punwani S. First-in-human in vivo non-invasive assessment of intra-tumoral metabolic heterogeneity in renal cell carcinoma. BJR|case reports 2019;5(3):20190003. [PubMed: 31428445]
40. Stødkilde-Jørgensen H, Laustsen C, Hansen ESS, Schulte R, Ardenkjaer-Larsen JH, Comment A, Frøkiær J, Ringgaard S, Bertelsen LB, Ladekarl M, Weber B. Pilot Study Experiences With Hyperpolarized [1–13C]pyruvate MRI in Pancreatic Cancer Patients. Journal of Magnetic Resonance Imaging 2019;0(0).
41. Reeder SB, Pineda AR, Wen Z, Shimakawa A, Yu H, Brittain JH, Gold GE, Beaulieu CH, Pelc NJ. Iterative decomposition of water and fat with echo asymmetry and least-squares estimation (IDEAL): Application with fast spin-echo imaging. Magnetic Resonance in Medicine 2005;54(3):636–644. [PubMed: 16092103]
42. Reeder SB, Brittain JH, Grist TM, Yen Y-F. Least-squares chemical shift separation for 13C metabolic imaging. Journal of Magnetic Resonance Imaging 2007;26(4):1145–1152. [PubMed: 17896366]
43. Wiesinger F, Weidl E, Menzel MI, Janich MA, Khegai O, Glaser SJ, Haase A, Schwaiger M, Schulte RF. IDEAL spiral CSI for dynamic metabolic MR imaging of hyperpolarized [1–13C]pyruvate. Magnetic Resonance in Medicine 2012;68(1):8–16. [PubMed: 22127962]

44. Brodsky EK, Holmes JH, Yu H, Reeder SB. Generalized k-space decomposition with chemical shift correction for non-cartesian water-fat imaging. Magnetic Resonance in Medicine 2008;59(5):1151–1164. [PubMed: 18429018]
45. Gordon JW, Niles DJ, Fain SB, Johnson KM. Joint spatial-spectral reconstruction and k-t spirals for accelerated 2D spatial/1D spectral imaging of 13C dynamics. Magnetic Resonance in Medicine 2014;71(4):1435–1445. [PubMed: 23716402]
46. Wiens CN, Friesen-Waldner LJ, Wade TP, Sinclair KJ, McKenzie CA. Chemical shift encoded imaging of hyperpolarized 13C pyruvate. Magnetic Resonance in Medicine 2015;74(6):1682–1689. [PubMed: 25427313]
47. Niles DJ, Gordon JW, Huang G, Reese S, Adamson EB, Djamali A, Fain SB. Evaluation of renal metabolic response to partial ureteral obstruction with hyperpolarized 13C MRI. NMR in Biomedicine 2017;31(1):e3846.
48. Lau AZ, Miller JJ, Robson MD, Tyler DJ. Simultaneous assessment of cardiac metabolism and perfusion using copolarized [1–13C]pyruvate and 13C-urea. Magnetic Resonance in Medicine 2017;77(1):151–158. [PubMed: 26743440]
49. Durst M, Koellisch U, Frank A, Rancan G, Gringeri CV, Karas V, Wiesinger F, Menzel MI, Schwaiger M, Haase A, Schulte RF. Comparison of acquisition schemes for hyperpolarised 13C imaging. NMR in Biomedicine 2015;28:715–725. [PubMed: 25908233]
50. Grist JT, McLean MA, Riemer F, Schulte RF, Deen SS, Zaccagna F, Woitek R, Daniels CJ, Kaggie JD, Matys T, Patterson I, Slough R, Gill AB, Chhabra A, Eichenberger R, Laurent M-C, Comment A, Gillard JH, Coles AJ, Tyler DJ, Wilkinson I, Basu B, Lomas DJ, Graves MJ, Brindle KM, Gallagher FA. Quantifying normal human brain metabolism using hyperpolarized [1–13C]pyruvate and magnetic resonance imaging. NeuroImage 2019;189:171–179. [PubMed: 30639333]
51. Liang Z Spatiotemporal imaging with partially separable functions. IEEE International Symposium on Biomedical Imaging: From Nano to Macro 2007:988–991.
52. Haldar JP, Liang Z. Spatiotemporal imaging with partially separable functions: A matrix recovery approach. IEEE International Symposium on Biomedical Imaging: From Nano to Macro 2010:716–719.
53. Lee H, Song JE, Shin J, Joe E, Joo CG, Choi Y-S, Song H-T, Kim D-H. High resolution hyperpolarized 13C MRSI using SPICE at 9.4T. Magnetic Resonance in Medicine 2018;80(2):703–710. [PubMed: 29315780]
54. Lam F, Liang Z-P. A subspace approach to high-resolution spectroscopic imaging. Magnetic Resonance in Medicine 2014;71(4):1349–1357. [PubMed: 24496655]
55. Haldar JP, Hernando D, Song S-K, Liang Z-P. Anatomically constrained reconstruction from noisy data. Magnetic Resonance in Medicine 2008;59(4):810–818. [PubMed: 18383297]
56. Lam F, Ma C, Clifford B, Johnson CL, Liang Z-P. High-resolution 1H-MRSI of the brain using SPICE: Data acquisition and image reconstruction. Magnetic Resonance in Medicine 2016;76(4):1059–1070. [PubMed: 26509928]
57. Ma C, Lam F, Ning Q, Johnson CL, Liang Z-P. High-resolution 1H-MRSI of the brain using short-TE SPICE. Magnetic Resonance in Medicine 2017;77(2):467–479. [PubMed: 26841000]
58. Peng X, Lam F, Li Y, Clifford B, Liang Z-P. Simultaneous QSM and metabolic imaging of the brain using SPICE. Magnetic Resonance in Medicine 2018;79(1):13–21. [PubMed: 29067730]
59. Song J, Shin J, Lee H, Choi Y-s, Joo CG, Song H-T, Kim D-H. Dynamic Hyperpolarized 13C MRSI using the SPICE technique: A feasibility study. In Proceedings of the 26th Annual Meeting of ISMRM, Paris, France, 2018 Abstract 3067.
60. Meyer CH, Pauly JM, Macovskiand A, Nishimura DG. Simultaneous spatial and spectral selective excitation. Magnetic Resonance in Medicine 1990;15(2):287–304. [PubMed: 2392053]
61. Cunningham CH, Chen AP, Lustig M, Hargreaves BA, Lupo J, Xu D, Kurhanewicz J, Hurd RE, Pauly JM, Nelson SJ, Vigneron DB. Pulse sequence for dynamic volumetric imaging of hyperpolarized metabolic products. Journal of Magnetic Resonance 2008;193(1):139–146. [PubMed: 18424203]

62. Gordon JW, Vigneron DB, Larson PEZ. Development of a symmetric echo planar imaging framework for clinical translation of rapid dynamic hyperpolarized 13C imaging. Magnetic Resonance in Medicine 2017;77(2):826–832. [PubMed: 26898849]
63. Cunningham CH, Lau JY, Chen AP, Geraghty BJ, Perks WJ, Roifman I, Wright GA, Connelly KA. Hyperpolarized 13C Metabolic MRI of the Human Heart: Initial Experience. Circulation Research 2016.
64. Gordon JW, Chen H-Y, Autry A, Park I, Van Criekinge M, Mammoli D, Milshteyn E, Bok R, Xu D, Li Y, Aggarwal R, Chang S, Slater JB, Ferrone M, Nelson S, Kurhanewicz J, Larson PEZ, Vigneron DB. Translation of Carbon-13 EPI for hyperpolarized MR molecular imaging of prostate and brain cancer patients. Magnetic Resonance in Medicine 2018;0(0).
65. Larson PEZ, Kerr AB, Chen AP, Lustig MS, Zierhut ML, Hu S, Cunningham CH, Pauly JM, Kurhanewicz J, Vigneron DB. Multiband excitation pulses for hyperpolarized 13C dynamic chemical-shift imaging. Journal of Magnetic Resonance 2008;194(1):121–127. [PubMed: 18619875]
66. Sigfridsson A, Weiss K, Wissmann L, Busch J, Krajewski M, Batel M, Batsios G, Ernst M, Kozerke S. Hybrid multiband excitation multiecho acquisition for hyperpolarized 13C spectroscopic imaging. Magnetic Resonance in Medicine 2015;73(5):1713–1717. [PubMed: 24845417]
67. Lau AZ, Chen AP, Ghugre NR, Ramanan V, Lam WW, Connelly KA, Wright GA, Cunningham CH. Rapid multislice imaging of hyperpolarized 13C pyruvate and bicarbonate in the heart. Magnetic Resonance in Medicine 2010;64(5):1323–1331. [PubMed: 20574989]
68. Miller JJ, Lau AZ, Tyler DJ. Susceptibility-induced distortion correction in hyperpolarized echo planar imaging. Magnetic Resonance in Medicine 2018;79(4):2135–2141. [PubMed: 28722201]
69. Geraghty BJ, Lau JYC, Chen AP, Cunningham CH. Dual-Echo EPI sequence for integrated distortion correction in 3D time-resolved hyperpolarized 13C MRI. Magnetic Resonance in Medicine 2018;79(2):643–653. [PubMed: 28394085]
70. Wang J, Wright AJ, Hesketh RL, Hu D-e, Brindle KM. A referenceless Nyquist ghost correction workflow for echo planar imaging of hyperpolarized [1–13C]pyruvate and [1–13C]lactate. NMR in Biomedicine 2018;31(2):e3866.
71. Leupold J, Månsson S, Petersson JS, Hennig J, Wieben O. Fast multiecho balanced SSFP metabolite mapping of 1 H and hyperpolarized 13 C compounds. Magnetic Resonance Materials in Physics, Biology and Medicine 2009;22(4):251–256.
72. Milshteyn E, von Morze C, Gordon JW, Zhu Z, Larson PEZ, Vigneron DB. High spatiotemporal resolution bSSFP imaging of hyperpolarized [1–13C]pyruvate and [1–13C]lactate with spectral suppression of alanine and pyruvate-hydrate. Magnetic Resonance in Medicine 2018;80(3):1048–1060. [PubMed: 29451329]
73. Reed GD, von Morze C, Bok R, Koelsch BL, Van Criekinge M, Smith KJ, Shang H, Larson PE, Kurhanewicz J, Vigneron DB. High Resolution 13C MRI With Hyperpolarized Urea: In Vivo T2 Mapping and 15N Labeling Effects. IEEE transactions on medical imaging 2014;33(2):362–371. [PubMed: 24235273]
74. Shang H, Sukumar S, Morze C, Bok RA, Marco-Rius I, Kerr A, Reed GD, Milshteyn E, Ohliger MA, Kurhanewicz J, Larson PEZ, Pauly JM, Vigneron DB. Spectrally selective three-dimensional dynamic balanced steady-state free precession for hyperpolarized C-13 metabolic imaging with spectrally selective radiofrequency pulses. Magnetic Resonance in Medicine 2016;78(3):963–975. [PubMed: 27770458]
75. Milshteyn E, von Morze C, Reed GD, Shang H, Shin PJ, Zhu Z, Chen H-Y, Bok R, Goga A, Kurhanewicz J, Larson PEZ, Vigneron DB. Development of high resolution 3D hyperpolarized carbon-13 MR molecular imaging techniques. Magnetic Resonance Imaging 2017;38:152–162. [PubMed: 28077268]
76. Svensson J, Månsson S, Johansson E, Petersson JS, Olsson LE. Hyperpolarized 13C MR angiography using trueFISP. Magnetic Resonance in Medicine 2003;50(2):256–262. [PubMed: 12876701]
77. Le Roux P Simplified model and stabilization of SSFP sequences. Journal of Magnetic Resonance 2003;163(1):23–37. [PubMed: 12852904]

78. Varma G, Wang X, Vinogradov E, Bhatt RS, Sukhatme VP, Seth P, Lenkinski RE, Alsop DC, Grant AK. Selective spectroscopic imaging of hyperpolarized pyruvate and its metabolites using a single-echo variable phase advance method in balanced SSFP. Magnetic Resonance in Medicine 2016;76:1102–1115. [PubMed: 26507361]

79. Reed GD, von Morze C, Addy NO, Ingle RR, Johnson KO, Overall WR, Hu BS, Vigneron DB, Larson PE, Santos JM. High spatiotemporal resolution hyperpolarized 13C angiography. Journal of Cardiovascular Magnetic Resonance 2016;18(1):Q30.

80. Hansen ESS, Stewart NJ, Wild JM, Stødkilde-Jørgensen H, Laustsen C. Hyperpolarized 13C,15N2-Urea MRI for assessment of the urea gradient in the porcine kidney. Magnetic Resonance in Medicine 2016;76(6):1895–1899. [PubMed: 27670826]

81. Månsson S, Petersson JS, Scheffler K. Fast metabolite mapping in the pig heart after injection of hyperpolarized 13C-pyruvate with low-flip angle balanced steady-state free precession imaging. Magnetic Resonance in Medicine 2012;68(6):1894–1899. [PubMed: 22294528]

82. von Morze C, Sukumar S, Reed GD, Larson PEZ, Bok RA, Kurhanewicz J, Vigneron DB. Frequency-specific SSFP for hyperpolarized 13C metabolic imaging at 14.1 T. Magnetic Resonance Imaging 2013;31(2):163–170. [PubMed: 22898680]

83. Sukumar S, Keshari KR, Bok R, Zhang V, Taylor A, Ohliger M, Yoshihara H, Kurhanewicz J, Vigneron Daniel B. Single-shot, Frequency and Time Specific, 3D Imaging Method for Measuring Hyperpolarized 13C Biomarkers InVivo at 14.1 Tesla. In Proceedings of the 19th Annual Meeting of ISMRM, Montreal, Canada, 2011 Abstract 3531.

84. Yen Y, Le Roux P, Mayer D, Takahashi A, Tropp J, Spielholz C, Pfefferbaum A, Hurd R. Exploring Multi-Shot Non-CPMG for Hyperpolarized 13C Metabolic MR Spectroscopic Imaging. In Proceedings of the 18th Annual Meeting of ISMRM, Stockholm, Sweden, 2010 Abstract 1015.

85. Wang J, Wright AJ, Hu D-e, Hesketh R, Brindle KM. Single shot three-dimensional pulse sequence for hyperpolarized 13C MRI. Magnetic Resonance in Medicine 2017;77(2):740–752. [PubMed: 26916384]

86. Wang J, Hesketh RL, Wright AJ, Brindle KM. Hyperpolarized 13C spectroscopic imaging using single-shot 3D sequences with unpaired adiabatic refocusing pulses. NMR in Biomedicine 2018;31(11):e4004. [PubMed: 30198124]

87. McLean MA, Grist JT, Zaccagna F, Riemer F, Madhu B, Laustsen C, Schulte RF, Graves MJ, Brindle Kevin M, Gallagher FA. Frequency calibration methods for the use of 13C spectral-spatial pulses in human brain. In Proceedings of the 27th Annual Meeting of ISMRM, Montreal, Quebec, 2018 Abstract 4297.

88. Xing Y, Reed GD, Pauly JM, Kerr AB, Larson PEZ. Optimal variable flip angle schemes for dynamic acquisition of exchanging hyperpolarized substrates. Journal of Magnetic Resonance 2013;234(0):75–81. [PubMed: 23845910]

89. Nagashima K Optimum pulse flip angles for multi-scan acquisition of hyperpolarized NMR and MRI. Journal of Magnetic Resonance 2008;190(2):183–188. [PubMed: 18023219]

90. Zhao L, Mulkern R, Tseng C-H, Williamson D, Patz S, Kraft R, Walsworth RL, Jolesz FA, Albert MS. Gradient-Echo Imaging Considerations for Hyperpolarized129Xe MR. Journal of Magnetic Resonance, Series B 1996;113(2):179–183.

91. Maidens J, Gordon JW, Arcak M, Larson PEZ. Optimizing flip angles for metabolic rate estimation in hyperpolarized carbon-13 MRI. IEEE Transactions on Medical Imaging 2016;PP(99):1–1. [PubMed: 26151933]

92. Durst M, Koellisch U, Gringeri C, Janich MA, Rancan G, Frank A, Wiesinger F, Menzel MI, Haase A, Schulte RF. Bolus tracking for improved metabolic imaging of hyperpolarised compounds. Journal of Magnetic Resonance 2014;243(0):40–46. [PubMed: 24717443]

93. Larson PEZ, Chen H-Y, Gordon JW, Korn N, Maidens J, Arcak M, Tang S, Criekinge M, Carvajal L, Mammoli D, Bok R, Aggarwal R, Ferrone M, Slater JB, Nelson SJ, Kurhanewicz J, Vigneron DB. Investigation of analysis methods for hyperpolarized 13C-pyruvate metabolic MRI in prostate cancer patients. NMR in Biomedicine 2018;0(0):e3997.

94. Gillies RJ, Schomack PA, Secomb TW, Raghunand N. Causes and Effects of Heterogeneous Perfusion in Tumors. Neoplasia 1999;1(3):197–207. [PubMed: 10935474]

95. Tang S, Milshteyn E, Reed G, Gordon J, Bok R, Zhu X, Zhu Z, Vigneron DB, Larson PEZ. A regional bolus tracking and real-time B1 calibration method for hyperpolarized 13C MRI. Magnetic Resonance in Medicine 2018;0(0).
96. Gordon JW, Larson PEZ. Pulse Sequences for Hyperpolarized MRS. eMagRes 2016.
97. Walker CM, Fuentes D, Larson PEZ, Kundra V, Vigneron DB, Bankson JA. Effects of excitation angle strategy on quantitative analysis of hyperpolarized pyruvate. Magnetic Resonance in Medicine 2019;0(0).
98. Maidens J, Gordon JW, Chen H, Park I, Criekinge MV, Milshteyn E, Bok R, Aggarwal R, Ferrone M, Slater JB, Kurhanewicz J, Vigneron DB, Arcak M, Larson PEZ. Spatio-temporally constrained reconstruction for hyperpolarized carbon-13 MRI using kinetic models. IEEE Transactions on Medical Imaging 2018;37(12):2603–2612. [PubMed: 29994332]
99. Hänicke W, Merboldt KD, Chien D, Gyngell ML, Bruhn H, Frahm J. Signal strength in subsecond FLASH magnetic resonance imaging: The dynamic approach to steady state. Medical Physics 1990;17(6):1004–1010. [PubMed: 2280729]
100. Gordon JW, Milshteyn E, Marco-Rius I, Ohliger M, Vigneron DB, Larson PEZ. Mis-estimation and bias of hyperpolarized apparent diffusion coefficient measurements due to slice profile effects. Magnetic Resonance in Medicine 2016:DOI: 10.1002/mrm.26482.
101. Deppe MH, Teh K, Parra-Robles J, Lee KJ, Wild JM. Slice profile effects in 2D slice-selective MRI of hyperpolarized nuclei. Journal of Magnetic Resonance 2010;202(2):180–189. [PubMed: 19969495]
102. Dominguez-Viqueira W, Geraghty BJ, Lau JYC, Robb FJ, Chen AP, Cunningham CH. Intensity correction for multichannel hyperpolarized 13C imaging of the heart. Magnetic Resonance in Medicine 2016;75(2):859–865. [PubMed: 26619820]
103. Hansen RB, Sánchez-Heredia JD, Bøgh N, Hansen ESS, Laustsen C, Hanson LG, Ardenkjær-Larsen JH. Coil profile estimation strategies for parallel imaging with hyperpolarized 13C MRI. Magnetic Resonance in Medicine 2019;82(6):2104–2117. [PubMed: 31297868]
104. Arunachalam A, Whitt D, Fish K, Giaquinto R, Piel J, Watkins R, Hancu I. Accelerated spectroscopic imaging of hyperpolarized C-13 pyruvate using SENSE parallel imaging. NMR in Biomedicine 2009;22(8):867–873. [PubMed: 19489035]
105. Jiang W, Lustig M, Larson PEZ. Concentric rings K-space trajectory for hyperpolarized 13C MR spectroscopic imaging. Magnetic Resonance in Medicine 2016;75(1):19–31. [PubMed: 25533653]
106. Shin PJ, Larson PEZ, Ohliger MA, Elad M, Pauly JM, Vigneron DB, Lustig M. Calibrationless parallel imaging reconstruction based on structured low-rank matrix completion. Magnetic Resonance in Medicine 2014;72(4):959–970. [PubMed: 24248734]
107. Gordon JW, Hansen RB, Shin PJ, Feng Y, Vigneron DB, Larson PEZ. 3D hyperpolarized C-13 EPI with calibrationless parallel imaging. Journal of Magnetic Resonance 2018;289:92–99. [PubMed: 29476930]
108. Lau AZ, Lau JYC, Chen AP, Cunningham CH. Simultaneous multislice acquisition without trajectory modification for hyperpolarized 13C experiments. Magnetic Resonance in Medicine 2018;80(4):1588–1594. [PubMed: 29427366]
109. Ohliger MA, Sodickson DK. An introduction to coil array design for parallel MRI. NMR in Biomedicine 2006;19(3):300–315. [PubMed: 16705631]
110. Lustig M, Donoho D, Pauly JM. Sparse MRI: The application of compressed sensing for rapid MR imaging. Magn Reson Med 2007;58(6):1182–1195. [PubMed: 17969013]
111. Hu S, Lustig M, Balakrishnan A, Larson PEZ, Bok R, Kurhanewicz J, Nelson SJ, Goga A, Pauly JM, Vigneron DB. 3D compressed sensing for highly accelerated hyperpolarized (13)C MRSI with in vivo applications to transgenic mouse models of cancer. Magn Reson Med 2010;63(2):312–321. [PubMed: 20017160]
112. Hu S, Balakrishnan A, Bok RA, Anderton B, Larson PEZ, Nelson SJ, Kurhanewicz J, Vigneron DB, Goga A. 13C-pyruvate imaging reveals alterations in glycolysis that precede c-Myc-induced tumor formation and regression. Cell Metab 2011;14(1):131–142. [PubMed: 21723511]

113. Cao P, Shin PJ, Park I, Najac C, Marco-Rius I, Vigneron DB, Nelson SJ, Ronen SM, Larson PEZ. Accelerated high-bandwidth MR spectroscopic imaging using compressed sensing. Magnetic Resonance in Medicine 2016;76(2):369–379. [PubMed: 27228088]

114. Wespi P, Steinhauser J, Kwiatkowski G, Kozerke S. High-resolution hyperpolarized metabolic imaging of the rat heart using k–t PCA and k–t SPARSE. NMR in Biomedicine 2018;31(2):e3876.

115. Geraghty BJ, Lau JYC, Chen AP, Cunningham CH. Accelerated 3D echo-planar imaging with compressed sensing for time-resolved hyperpolarized 13C studies. Magnetic Resonance in Medicine 2016:DOI: 10.1002/mrm.26125.

116. Yen Y-F, Le Roux P, Mayer D, King R, Spielman D, Tropp J, Butts Pauly K, Pfefferbaum A, Vasanawala S, Hurd R. T2 relaxation times of 13C metabolites in a rat hepatocellular carcinoma model measured in vivo using 13C-MRS of hyperpolarized [1–13C]pyruvate. NMR in Biomedicine 2010;23(4):414–423. [PubMed: 20175135]

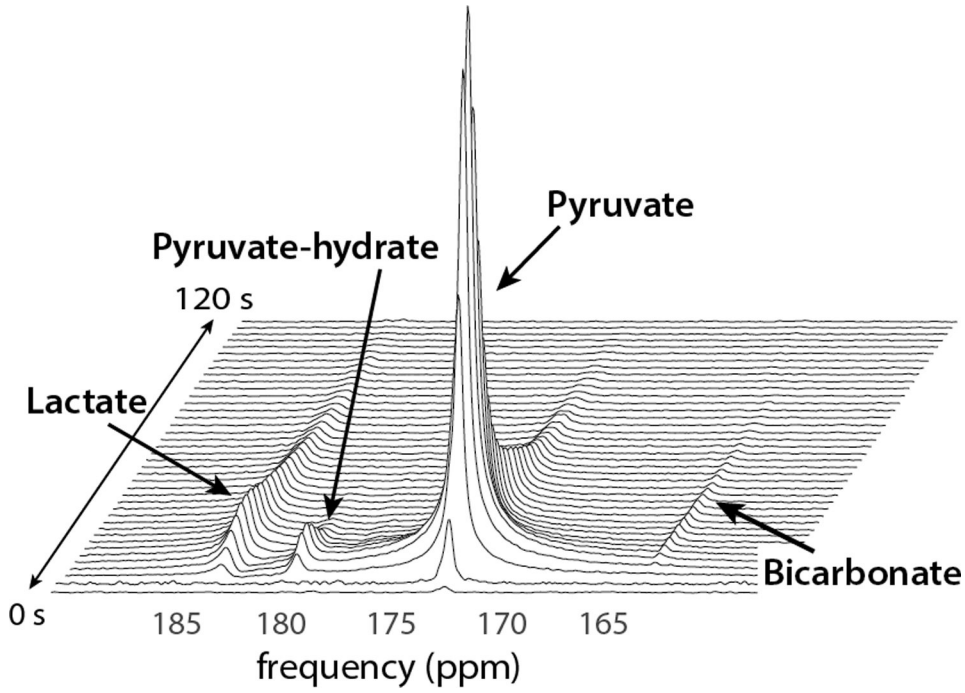

Figure 1:

Representative dynamic HP-^{13}C spectra illustrates the metabolic conversion of the injected substrate ([1-^{13}C]pyruvate) into products of interest ([1-^{13}C]lactate, [^{13}C]bicarbonate, and [1-^{13}C]pyruvate-hydrate) in the human brain. Conversion to alanine is also observable within the timescale of the experiment in other organs. Their temporal profiles reflect the rapid enzymatic conversion of pyruvate throughout the timeframe of HP-^{13}C studies. Figure adapted from Ref. (33).

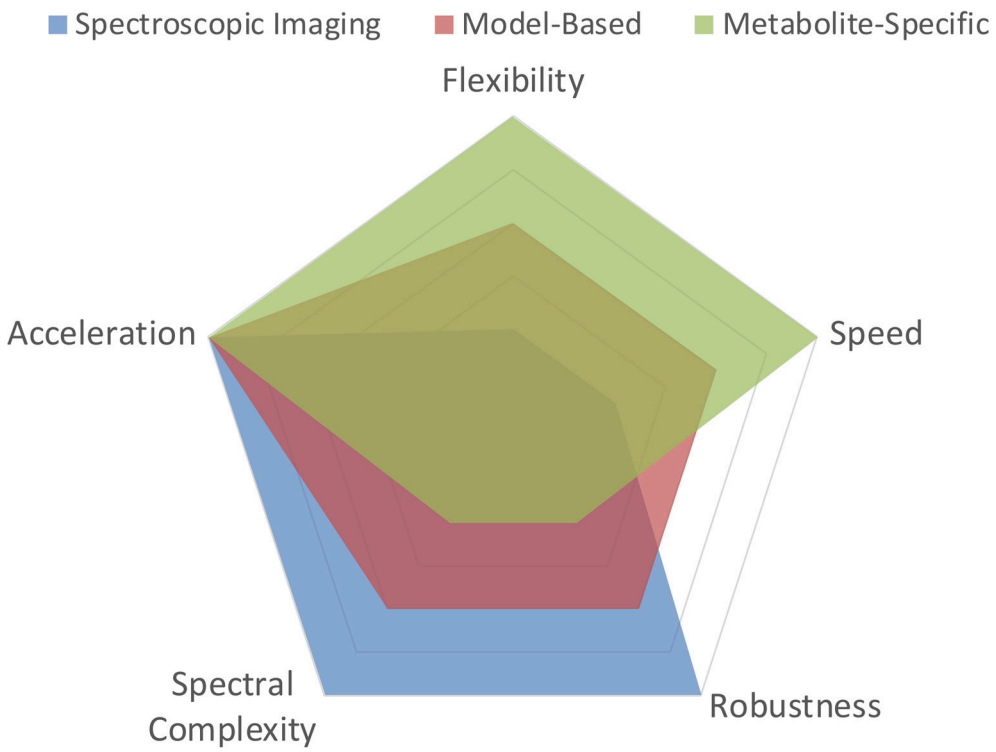

Figure 2:

Overview of the main categories of fast hyperpolarized metabolic imaging methods and their corresponding advantages and disadvantages. Acceleration refers to compatibility with compressed sensing/parallel imaging; Flexibility refers to the available acquisition and tailored flip angle schemes; Speed refers to acquisition time; Robustness refers to sensitivity to bulk frequency errors and B0 inhomogeneity; Spectral complexity refers to compatibility with substrates that have complicated spectra (i.e. numerous resonances, poor spectral separation, j-coupling, etc.). The tradeoffs between the categories are described in greater detail in Table 1 as well as throughout the text.

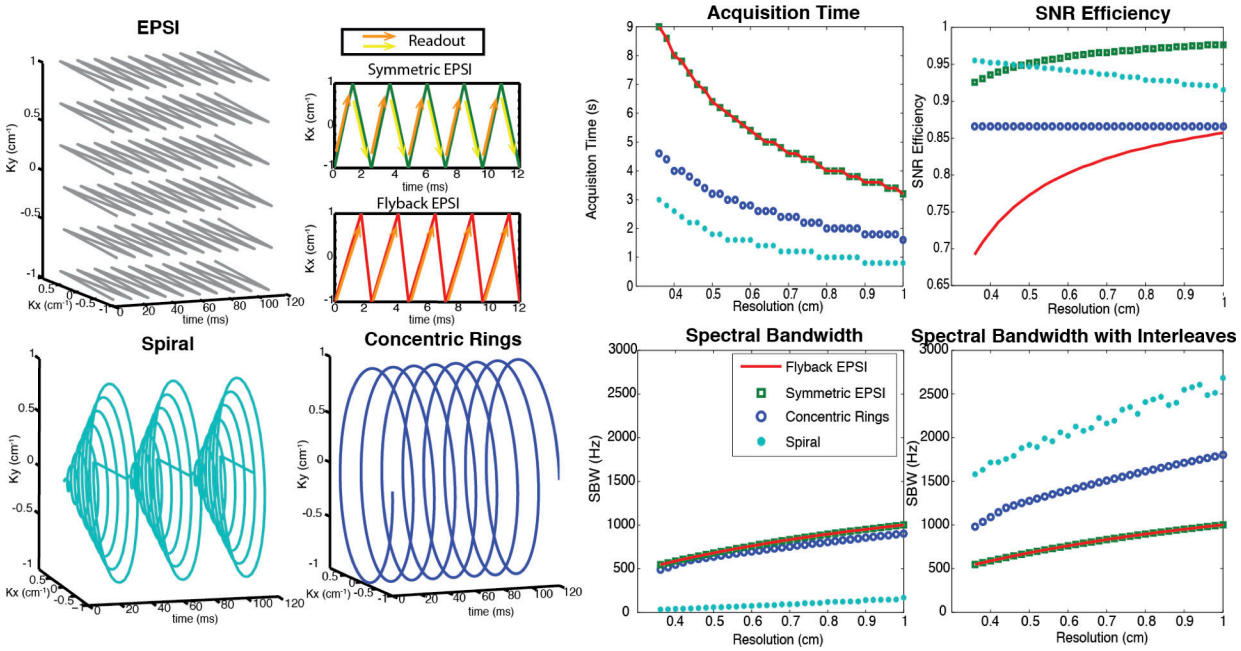

Figure 3:

Illustration and comparison of several rapid MRSI methods employing switched/time-dependent read-out gradients. Left two columns: k-space trajectories for EPSI (symmetric and flyback), spiral and concentric rings spectroscopic imaging. Right two columns: Design tradeoffs between spatial resolution, spectral bandwidth, acquisition time, and SNR efficiency, assuming typical clinical MRI system gradients with a maximum amplitude of 40 mT/m and maximum slew rate of 150 mT/m/ms. EPSI is the slowest, but symmetric EPSI trajectories have very high SNR efficiency. The concentric rings method requires half of the total acquisition time compared with the EPSI trajectories, offers about 87% SNR efficiency, and provides much wider spectral bandwidth than either flyback or symmetric EPSI. Although spirals are nominally the most efficient trajectories (offering the fastest acquisition time and highest spectral bandwidth while sacrificing the least SNR), they are limited by their sensitivity to gradient infidelities. (Adapted from Ref (25)).

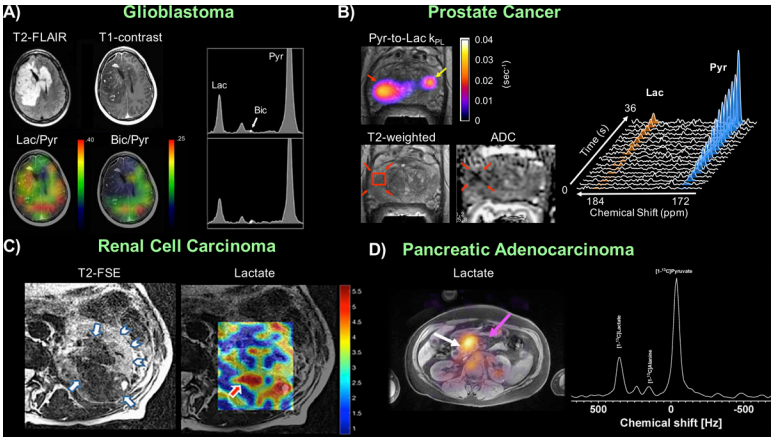

Figure 4:

Proof-of-concept human studies based on fast spectroscopic imaging approaches applied in (A) Brain tumor (B) Primary prostate cancer (C) Renal cell carcinoma and (D) Pancreatic cancer with example images and spectra, highlighting the ability to extract spatially-resolved information of metabolism without a priori knowledge of the product identities. Figure adapted from (33,37,39,40).

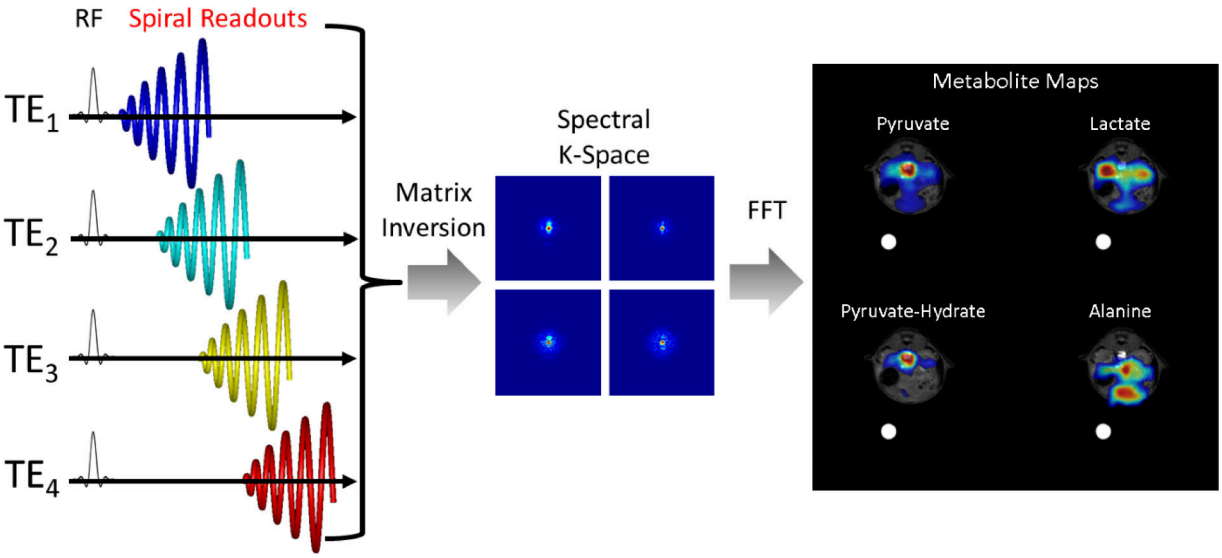

Figure 5:

Schematic illustrating the acquisition and reconstruction of a model-based spiral pulse sequence. In this illustration, data is acquired with a long duration spiral readout that is spoiled at each TR. Each subsequent excitation is shifted in time by ΔTE. For non-Cartesian approaches, a matrix decomposition occurs in k-space, yielding k-space data for each metabolite. A subsequent gridding or non-uniform fast Fourier Transform (nuFFT) step yields spectral images for each hyperpolarized metabolite.

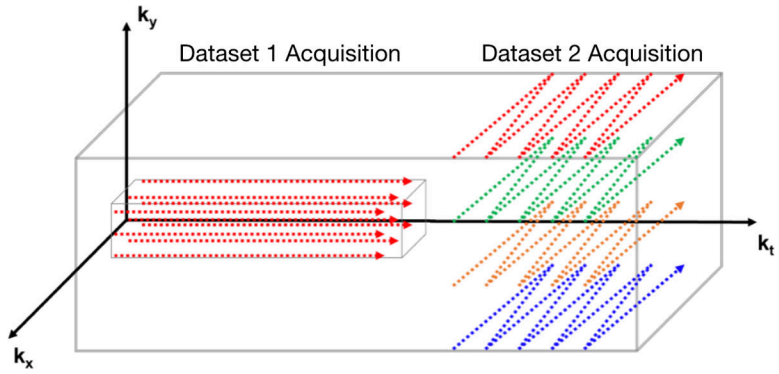

Figure 6:

Graphical depiction of the SPICE acquisition. The acquisition is comprised of two stages. The first stage acquires a low-spatial resolution/high spectral bandwidth dataset (D1) with a CSI sequence. The data of this stage is used to identify the spectral signals images. The second stage acquires a high-spatial resolution/low spectral bandwidth dataset (D2) with an EPSI sequence. These two datasets are combined to generate spectroscopic images with high spatial and spectral resolution.

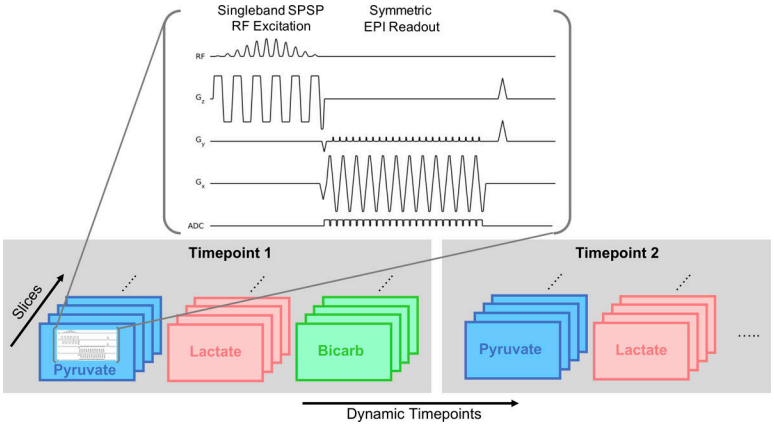

Figure 7:

Depiction of a multi-slice metabolite-specific acquisition using EPI. The sequence provides volumetric coverage for all metabolites of interest by shifting the spectral-spatial (SPSP) passband to separately excite and encode each resonance. This is repeated through time to acquire a volumetric and dynamic dataset for all metabolites of interest. Figure adapted from (62).

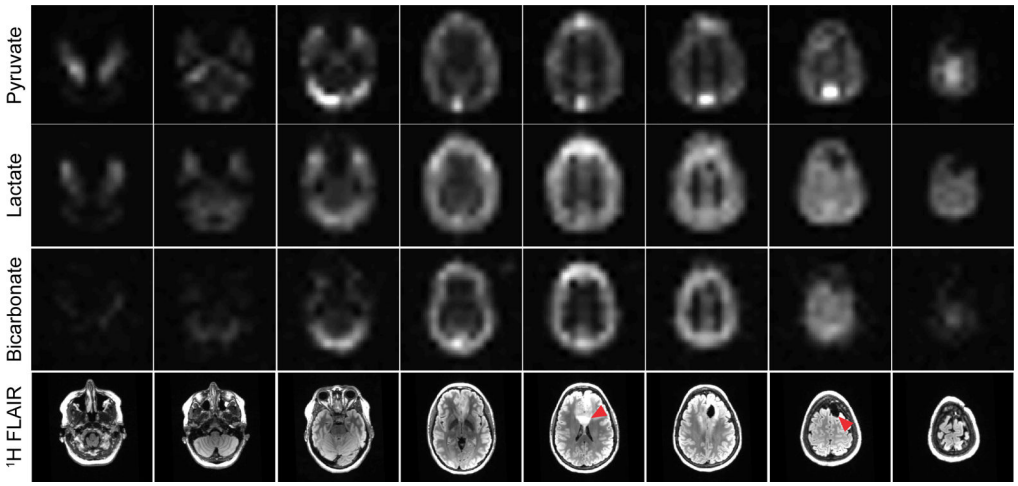

Figure 8:

Area under the curve (sum through time) images of pyruvate, lactate, and bicarbonate for the eight slices covering the entire brain. In this experiment, a spectral-spatial RF pulse was used to separately excite each metabolite, which was then encoded with a single-shot echoplanar readout. Artifact-free data can be acquired with rapid imaging readouts in the clinical setting, enabling volumetric coverage of the whole brain with a temporal resolution (3 s) equivalent to that of single slice EPSI. Figure adapted from Ref (64).

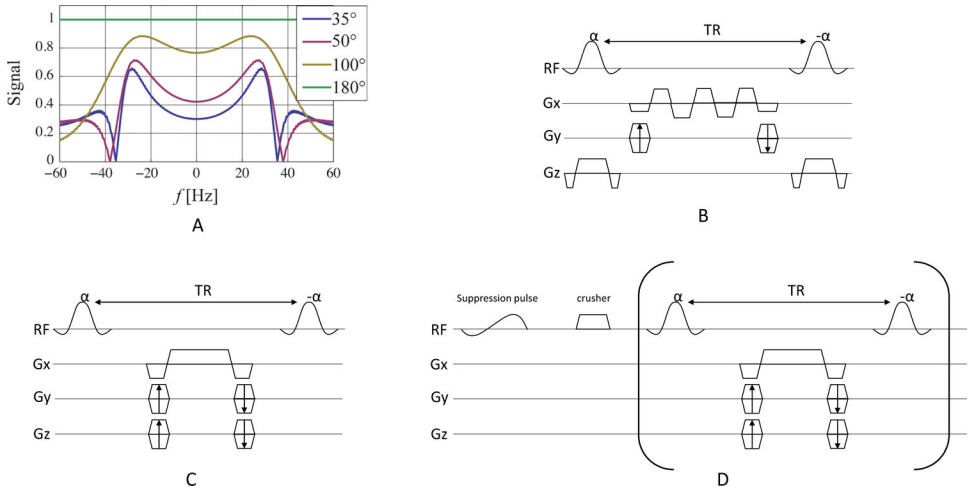

Figure 9:

Simulated SSFP signal as a function of frequency and flip angle for TR = 14.3 ms (A). The choice of flip angle in the bSSFP sequence is a tradeoff between alleviating banding artifacts with high flip angles and preserving magnetization for dynamic imaging with lower flip angles. Pulse sequence diagrams for bSSFP, including (B) multi-echo readouts to decompose spectral information, (C) metabolite specific acquisition, and (D) metabolite specific acquisition with spectral suppression of undesired signal at the beginning of the acquisition. Portions of this figure are adapted from Ref. (73).

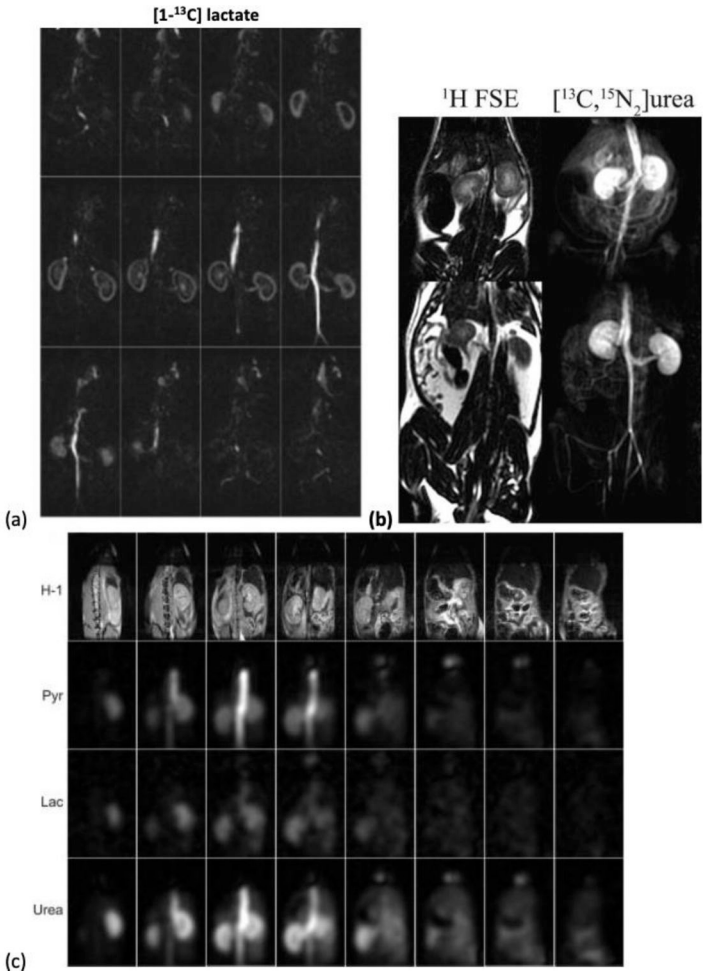

Figure 10:

Representative bSSFP results from prior works. (a) Rat 3D kidney images of [1-^{13}C]lactate at 3T (75) (b) Rat kidney projection image of [^{13}C-, $^{15}N_2$]urea at 3T (73). (c) 3D kidney images of co-polarized [1-^{13}C]pyruvate and [^{13}C, $^{15}N_2$]urea at 14 T (74).

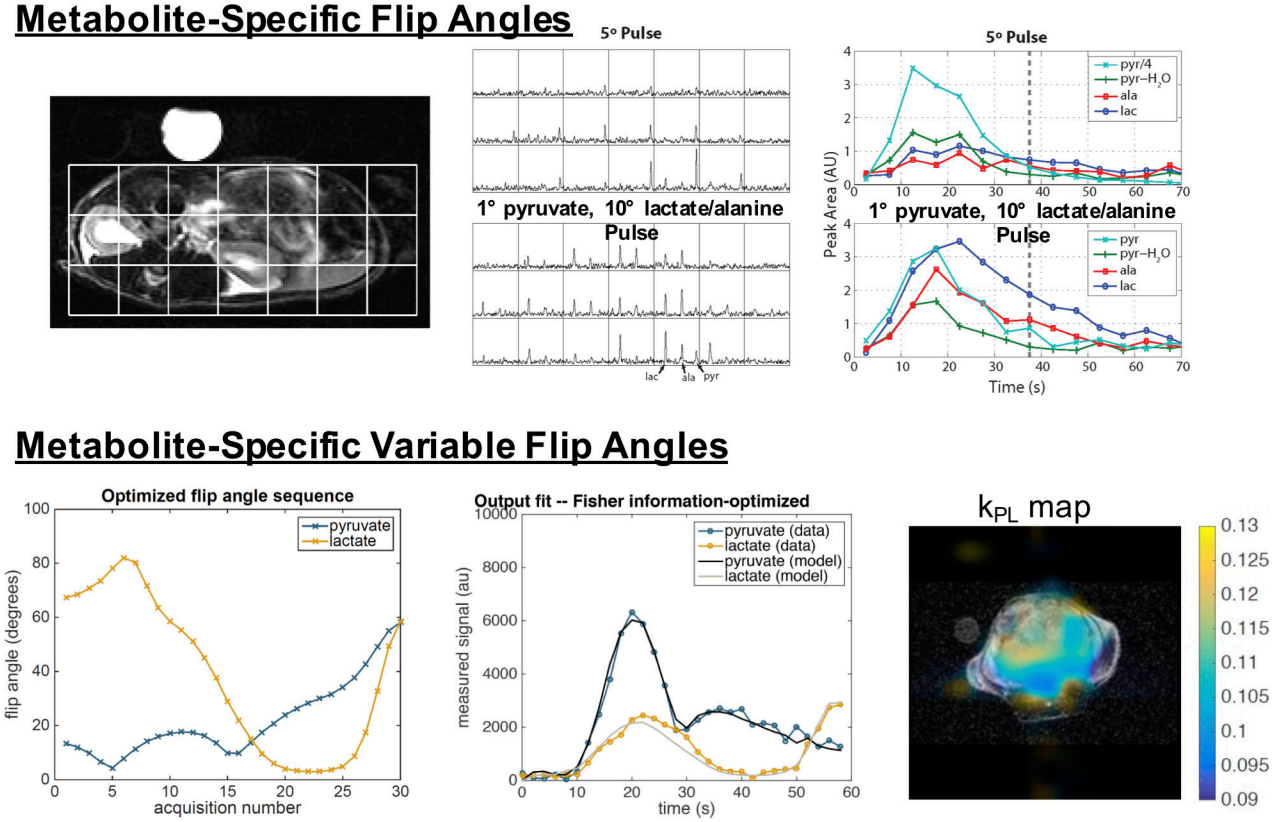

Figure 11:

(top) Metabolite-specific flip angles, implemented in a MRSI acquisition using multiband spectral-spatial RF pulses, show substantial improvements over constant flip angle pulses. In this example, the multiband pulse applied a 1-degree flip angle to pyruvate (substrate) and 10-degree flip angle to the metabolic products of lactate and alanine to improve their SNR while maintaining adequate pyruvate SNR (65). (bottom) A metabolite-specific variable flip angle schedule implemented in a metabolite-specific EPI acquisition, optimized for estimation of the pyruvate to lactate conversion rate, k_{PL} for an expected set of experimental parameters. Fitting to data acquired with metabolite-specific imaging and the resulting k_{PL} map in a prostate tumor mouse show high quality fits (91).

Table 1.

Strengths and weaknesses of the three main imaging methods for hyperpolarized ^{13}C MRI.

Method Category	Pros	Cons
Fast Spectroscopic Imaging	No prior knowledge of spectrum required. Insensitive to B0.	Slower than other methods.
Model-based/hybrid Imaging	Rapid imaging of complex spectra.	Requires prior knowledge and model of the spectrum.
Metabolite-Specific Imaging	Very fast and RF efficient. Robust to motion.	Requires a sparse spectrum. Sensitive to B0 inhomogeneities.

Table 2:

Overview of additional sequence options that can be combined with the main categories of imaging techniques described in Table 1.

Sequence Options	Pros	Cons
Parallel Imaging	Accelerate acquisitions using multichannel receive arrays.	^{13}C coil sensitivities challenging to measure. g-factor SNR penalty.
Compressed Sensing	Accelerate acquisitions based on data sparsity.	Tuning of regularization parameters. Excessive denoising possible.
Tailored Flip Angles	Metabolite-specific flip angles to improve metabolic product SNR. Variable flip angles to increase overall SNR.	Increased sensitivity to perfusion variability and flip angle miscalibration.
Refocused Methods (Spin-echoes, SSFP)	Improve SNR with spin refocusing.	Refocusing pulses introduce B1+ sensitivity and saturation. Dynamic imaging is challenging.
Real-time Calibration	More reproducible results with timing, B0, and B1 calibration. B1+ maps improve SNR and accuracy of quantifications.	Utilizes HP magnetization (<5%) for calibration. Requires highly specialized pulse programs. Delays start of main acquisition.